Received NNN; | Revised NNN; | Accepted NNN

DOI: xxx/xxxx

RESEARCH ARTICLE

A three-dimensional macroelement for modelling the in-plane and out-of-plane response of masonry walls

Francesco Vanin[1] | Andrea Penna[2] | Katrin Beyer*[1]

[1]Earthquake Engineering and Structural Dynamics Laboratory (EESD), École Polytechnique Fédérale de Lausanne (EPFL), Lausanne, Switzerland

[2]Department of Civil Engineering and Architecture, University of Pavia, European Centre for Training and Research in Earthquake Engineering, Pavia, Italy

Correspondence

*Katrin Beyer, Earthquake Engineering and Structural Dynamics Laboratory (EESD), School of Architecture, Civil and Environmental Engineering (ENAC), École Polytechnique Fédérale de Lausanne (EPFL), EPFL ENAC IIC EESD, GC B2 495, Station 18, CH-1015 Lausanne, Switzerland.
Email: katrin.beyer@epfl.ch

Summary

The seismic performance of unreinforced masonry buildings is commonly assessed using equivalent frame modelling. Its computational efficiency allows for a large number of analyses to be conducted, which are often required to account for epistemic and aleatoric uncertainties. To obtain a full description of the building response, in-plane and out-of-plane failure modes need to be considered, though previous elements for equivalent frame models of unreinforced masonry buildings only account for the in-plane response. This paper presents the formulation of a three-dimensional macroelement for modelling the dynamic in-plane and out-of-plane behaviour of masonry panels, which extends the approach of a previously developed macroelement to simulate the in-plane response. The proposed three-node, three-dimensional macroelement is implemented in the software OpenSees and describes the main features of the in-plane and out-of-plane behaviour of a masonry wall, including second-order geometrical effects and a coupled shear/flexural response. It also allows for the use of complex material models. The proposed element is used to simulate experimental results for in-plane shear-compression tests and out-of-plane free vibration tests of masonry panels. The implemented element, as well as the example models, are openly shared through the repository https://github.com/eesd-epfl/OpenSees/wiki.

KEYWORDS:
3D macroelement; equivalent frame modelling; out-of-plane response; masonry; seismic analysis

1 | INTRODUCTION

Unreinforced masonry buildings are among the most vulnerable under earthquake loading, and as such, are responsible for much of the economic and social impact of a seismic event. Since their seismic behaviour is heavily influenced by nonlinear phenomena, such as cracking or crushing, that is already apparent at moderate deformation levels, it is common to conduct nonlinear seismic analyses when assessing or even designing such buildings. To assist in this regard, several approaches have been proposed in the literature for modelling structural masonry, varying in the level of detail. In detailed micro-modelling approaches [1], the heterogeneity of the material is treated explicitly, while in simplified micromodels, joints are modelled by interface elements [2,3]. Less computationally expensive models include homogenised micromodels [4,5,6] and models in which damage is smeared into a continuum [7,8,9]. As an alternative to finite element modelling, discrete elements have been used for blocky

structures[10,11], accounting for the complex dynamics of interacting blocks. Although such modelling approaches comprise different levels of complexity and are, as a result, applicable at different scales, the use of dynamic analyses for entire masonry buildings is still limited, especially in professional applications, mainly due to their considerable computational cost. In particular, the numerous sets of analyses needed to investigate the variability of the dynamic behaviour of a building for epistemic and aleatoric uncertainties[12,13] calls for models that are computationally very efficient. As a compromise between a sufficient level of accuracy and a limited computational cost, equivalent frame modelling[14,15,16,17,18] is a widely adopted choice for masonry buildings (see Quagliarini et al.[19] for a comprehensive review). This modelling technique assumes that a masonry façade can be simplified into a frame of pier and spandrel elements connected by portions of masonry subjected to lower deformations and less prone to damage, which are generally considered to be rigid nodes. Such an approach can be applied if the façade layout is relatively regular; in this case, comparisons with experimental tests[20,21,22] and more detailed numerical analyses[23,24] have shown that equivalent frame models are a robust approach for modelling unreinforced masonry buildings.

Existing tools for the equivalent frame modelling of masonry buildings consider an assemblage of two-dimensional frames that represent the in-plane response of the masonry elements and neglect their out-of-plane behaviour[14,25]. The out-of-plane response is typically not critical if the walls are tied together at all storey levels. Particularly for historical buildings, however, this out-of-plane failure is often the cause of collapse and casualties[26]. When using equivalent frame models that do not capture the out-of-plane behaviour, other types of analyses (i.e. rigid body limit analysis of collapse mechanisms[27] or discrete element modelling[28,29,30]) have to also be performed. This necessarily assumes, however, that the in-plane and out-of-plane responses are not coupled. A more complex plane rectangular macroelement that is also applicable to shell structures and accounts for the out-of-plane behaviour was proposed by Caliò et al.[31]. In this approach, the building is modelled as an assemblage of panels, which can be used to describe any geometric layout, including vaults or complex geometries like churches[32]. This comes at a cost, though, as the inherent simplicity of equivalent frame modelling is partially lost. On the other hand, equivalent frame models with force-based beam elements[24,33,34,35] could theoretically model the out-of-plane response, though this has not yet been attempted. Furthermore, these analyses come with a certain increase in numerical complexity and, in their current implementation, cannot yet describe the dependency of the maximum shear capacity on the applied axial load[24,33,34,35].

Towards the development of equivalent frame models that allow this integrated assessment of a masonry building, this paper proposes a novel three-dimensional macroelement formulation that accounts for the main features of the in-plane and out-of-plane dynamic response and accounts for material and geometrical nonlinearity. The formulation is based on the macroelement developed by Penna et al.[25] for modelling the in-plane behaviour of masonry panels. The new element is implemented in the open-source software OpenSees[36] and is therefore freely and openly available to the research community, with extensive documentation and example models of masonry sub-assemblages and buildings shared through the repository "https://github.com/eesd-epfl/OpenSees/wiki". By integrating this model in OpenSees, future research can make use of the existing library of material models and element types, increasing the complexity of equivalent frame models of unreinforced masonry buildings or mixed building types that can be developed. To maximise the versatility of the element and investigate the effect of various modelling assumptions on the overall seismic response of a masonry building, this macroelement provides a choice of various section models, including fibre sections in combination with any uniaxial material laws, as well as between various shear models, mass discretisations and damping models. Moreover, the macroelement comprises a versatile drift capacity model, with which the drift capacity at the loss of the horizontal load-bearing capacity can be expressed as a function of the failure mode, axial load ratio and shear span to element height ratio. Additionally, the loss of the vertical load-bearing capacity at a drift, which is a multiple of the drift at horizontal load failure, can also be modelled. These modelling options have been implemented to facilitate sensitivity studies on modelling assumptions.

2 | MACROELEMENT FORMULATION

The macroelement is formulated as a one-dimensional element defined by three nodes, two at the element ends and one at midspan, all defined in three-dimensional space. It consists of an assemblage of two panels subjected to the same average shear deformation and separated by three nonlinear sections accounting for deformations due to axial strains. The kinematic of this element is presented in Figure 1. The shear response is controlled by a non-linear interface located at mid-height of the element, in which all shear deformations of the two panels are lumped (Figure 1b). The shear strength of the section is coupled to the axial load that acts on the mid-section. To decouple shear deformations from the axial deformations, and therefore avoid an iterative element state determination procedure to enforce equilibrium, a non-dilatant behaviour of the shear interface is postulated.

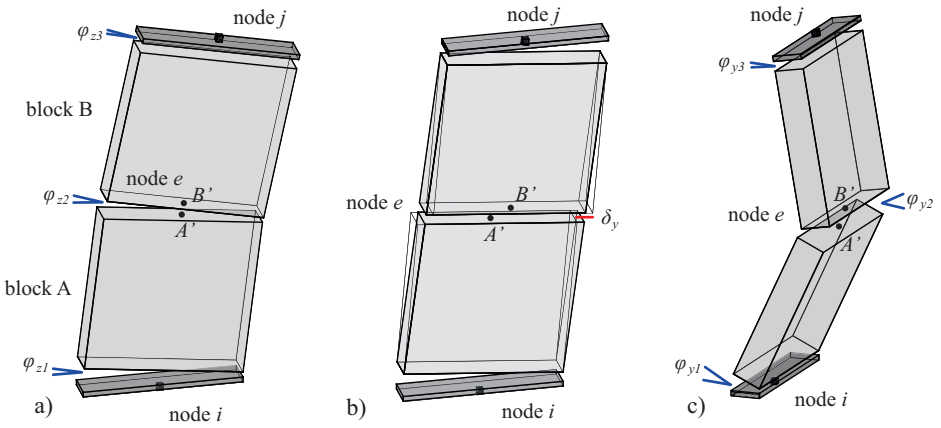

FIGURE 1 Deformation modes of the macroelement: (a) in-plane flexure only, (b) in-plane flexure and shear and (c) out-of-plane response.

The flexural response is described by three sections that can model coupled in-plane and out-of-plane rocking. The midspan section of the element allows the one-way out-of-plane bending to be modelled in a simplified way. The uplift related to the in-plane and out-of-plane flexural response can be properly described by suitable sectional models. This feature is particularly relevant, for example, if the macroelement is used to model piers coupled by RC slabs or spandrels in buildings with highly deformable floors, in which the axial deformations related to the flexural response can largely increase the axial load in the spandrels, and consequently, the shear force that such spandrels can transfer. Moreover, since mechanisms of the type in Figure 1c require an elongation of the element, the uplift in rocking needs to be modelled to capture the kinematic constraints against out-of-plane failure provided by stiff floor diaphragms, for example. The macroelement can therefore represent the out-of-plane failure of piers with transient static boundary conditions (e.g. change in axial load related to the rocking response of the pier) and transient kinematic boundary conditions (e.g. sliding or uplift of the floor).

The element nodes are located at the extremities and the midspan of the element, which allows for rigid offsets of the end nodes. The end nodes (named i and j in Figure 1) are standard three-dimensional nodes whose degrees of freedom describe three displacements and three rotations in space. The internal node e defines the displacements of the extremities of blocks A and B (points A' and B' in Figure 1) in three directions, from which the finite rotations of the two blocks can be derived. The degrees of freedom of the three nodes are arranged in the vector $\boldsymbol{u}_{\text{local}}$ (Figure 2a) as:

$$\begin{aligned}\boldsymbol{u_{local}} &= [u_i, v_i, w_i, \varphi_{xi}, \varphi_{yi}, \varphi_{zi}, \quad u_j, v_j, w_j, \varphi_{xj}, \varphi_{yj}, \varphi_{zj}, \quad u_A, v_A, w_A, u_B, v_B, w_B]^T,\\ \boldsymbol{q_{local}} &= [N_i, V_{yi}, V_{zi}, T_{xi}, M_{yi}, M_{zi}, \quad N_j, V_{yj}, V_{zj}, T_{xj}, M_{yj}, M_{zj}, \quad N_{eA}, V_{yA}, V_{zA}, N_{eB}, V_{yB}, V_{zB}]^T.\end{aligned} \tag{1}$$

From the vector of local displacements, the 12 displacements (Figure 2b) defining those at the flexural sections, the shear deformations of the panels and a constant torsional deformation along the element ($\boldsymbol{u}_{\text{basic}}$) can be obtained as:

$$\boldsymbol{u_{basic}}^{(\boldsymbol{P-\Delta})} = \begin{bmatrix} d_1 \\ \varphi_{z1} \\ \varphi_{y1} \\ d_2 \\ \varphi_{z2} \\ \varphi_{y2} \\ d_3 \\ \varphi_{z3} \\ \varphi_{y3} \\ s_y \\ s_z \\ \varphi_{tors} \end{bmatrix} = \begin{bmatrix} u_{eA} - u_i + \frac{(v_{eA}-v_i)^2+(w_{eA}-w_i)^2}{H} \\ -\varphi_{zi} - (v_{eA} - v_i)\frac{2}{H} \\ -\varphi_{yi} - (w_{eA} - w_i)\frac{2}{H} \\ -u_{uA} + u_{eB} \\ (-v_{eA} - v_{eB} + v_i + v_j)\frac{2}{H} \\ (w_{eA} + w_{eB} - w_i - w_j)\frac{2}{H} \\ -u_{eB} + u_j + \frac{(v_{eB}-v_j)^2+(w_{eB}-w_j)^2}{H} \\ \varphi_{zj} + (v_{eB} - v_j)\frac{2}{H} \\ \varphi_{yj} + (w_{eB} - w_j)\frac{2}{H} \\ v_{eB} - v_{eA} \\ w_{eB} - w_{eA} \\ \varphi_{xj} - \varphi_{xi} \end{bmatrix} \tag{2}$$

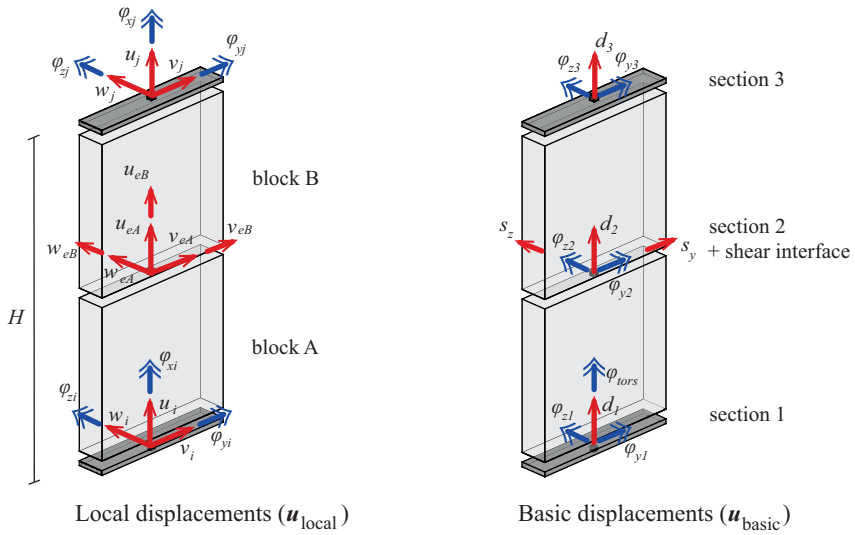

FIGURE 2 Definition of local and basic degrees of freedom of the macroelement.

The exact formulation of the compatibility relations, accounting for finite rotations in space, is reported in the supplemental materials (see Section 8). To avoid the complexity of the co-rotational formulation while still accounting for second-order effects for moderate displacements, the element was implemented using only a $P-\Delta$ formulation, expressed by Equation 2, derived as a second-order Taylor-series expansion of the exact equations. Second-order effects are typically less relevant for the in-plane behaviour of a masonry element, though must be considered when modelling its out-of-plane behaviour.

The section models adopted for the three flexural sections and the shear interface shown in Figure 2 provide the local response in terms of sectional forces and the stiffness matrices of these sections. The vector of basic forces $\boldsymbol{q}_{\text{basic}}$ is assembled as:

$$\boldsymbol{q_{basic}} = [N_1, M_{z1}, M_{y1}, \quad N_2, M_{z2}, M_{y2}, \quad N_3, M_{z3}, M_{y3}, \quad V_y, V_z, T_{tors}]. \tag{3}$$

The axial and flexural behaviour of each section i is described by three section models that relate a set of deformations $\boldsymbol{\varepsilon_i}$ (one axial deformation, ε_{0i}, and two curvatures, χ_{zi} and χ_{yi}) to the corresponding sectional forces $\boldsymbol{q_{basic,i}}$ for the i-th interface:

$$\boldsymbol{q_{basic,i}} = \begin{bmatrix} N_i \\ M_{zi} \\ M_{yi} \end{bmatrix} = \boldsymbol{q_{sect,i}}(\boldsymbol{\varepsilon_i}). \tag{4}$$

In addition to the sectional models, two shear interfaces describe the nonlinear in-plane and out-of-plane shear response through a biaxial material law that is coupled to the axial load applied to the middle section. The torsional behaviour, accounted for by the first section model, is modelled as linear elastic and is decoupled from all other behaviour modes, consistently with the implementation in OpenSees of the fibre section model used in nonlinear beams. Such approach is rather simplified but it is expected to have a minor impact on the global response of an equivalent frame model of a masonry building.

The basic displacements $\boldsymbol{u_{basic,i}} = [d_i, \varphi_{zi}, \varphi_{yi}]^T$ relative to the i-th flexural interface can be interpreted as the result of constant deformations $\boldsymbol{\varepsilon_i}$ integrated along a certain length of the macroelement $\overline{w}_i H$ if H is the total height of the element:

$$\boldsymbol{\varepsilon_i} = \begin{bmatrix} \varepsilon_{0i} \\ \chi_{zi} \\ \chi_{yi} \end{bmatrix} = \frac{1}{\overline{w}_i H} \begin{bmatrix} d_i \\ \varphi_{zi} \\ \varphi_{yi} \end{bmatrix} = \frac{1}{\overline{w}_i H} \boldsymbol{u_{basic,i}}. \tag{5}$$

In consequence, the stiffness matrix $\boldsymbol{K_i}$ relative to the interface i needs to therefore be derived from the stiffness of the sectional model $\boldsymbol{K_{sect,i}}$ as:

$$\boldsymbol{K_i} = \frac{\partial \boldsymbol{q_{basic,i}}}{\partial \boldsymbol{u_{basic,i}}} = \frac{1}{\overline{w}_i H} \frac{\partial \boldsymbol{q_{sect,i}}}{\partial \boldsymbol{\varepsilon_i}} = \frac{1}{\overline{w}_i H} \boldsymbol{K_{sect,i}}. \tag{6}$$

The portion of the macroelement attributed to each section can be assigned by the user, similarly to assigning weights to different integration points along the axis of a beam element. The weights can be chosen such that the flexural response of the macroelement exactly reproduces that of a force-based beam element with three integration points, since the equilibrium condition is strictly imposed at every section to avoid the potential force unbalance shown by displacement-based elements at the section level. The solution procedure avoids a nested internal iteration scheme because the equilibrium condition at the section level is directly imposed by the global iterative scheme. The optimum choice, in terms of correspondence between the behaviour of the macroelement and the solution of a beam subjected to a generic nonlinear curvature profile, is given by the set of weights $\overline{\boldsymbol{w_i}}$ of a Gauss-Lobatto integration scheme with three integration points, i.e. the set of weights $\left[1/6, 2/3, 1/6\right]$. Such a scheme leads to the exact integration of a polynomial of order three and is therefore assumed as default choice in the current OpenSees implementation of the element. The top displacements of the macroelement therefore correspond to the exact solution of a beam subjected to a parabolic curvature profile, clearly including the elastic solution when no element loads are applied. Other choices of integration weights are also possible; they can be related, for example, to the adoption of a user-defined plastic hinge length, improving the modelling of the nonlinear range at the cost of a lower accuracy of the linear elastic solution. Differing the choices that are set for the integration weights, however, should be justified by proper calibration against experimental data. The in-plane response of the macroelement designed by Penna et al.[25] and implemented in Tremuri is obtained under the assumption that only the two end sections can deform, which for some loading conditions, leads to a lower elastic element stiffness than that of an elastic beam. To reproduce the behaviour of the macroelement by Penna et al.[25] by the macroelement implemented in OpenSees, the following set of weights is used if the Tremuri-flag is activated: $\left[0.495, 0.01, 0.495\right]$. Note that all assigned weights must be positive, meaning therefore that the central interface should be assigned a positive negligible integration weight. With this integration scheme, neglecting the deformability of the central interface, the applied section model can simply be linear elastic.

For simplicity, the shear interface is split into two components, namely the in-plane component along the local axis y and the out-of-plane component along the local axis z. In the general formulation, the two components can be assigned two different shear models. Both shear models must be biaxial material models, describing the shear response as a function of a shear displacement s_y, s_z and an axial displacement s_n:

$$V_y = V_y(s_n, s_y), \quad V_z = V_z(s_n, s_z). \tag{7}$$

To model masonry elements, a nonlinear shear model, such as the one presented in Section 4, can be applied in the in-plane direction, and an elastic model can be applied in the out-of-plane direction, since the out-of-plane force capacity is controlled by the flexural behaviour. However, if the user imposes two nonlinear models for the two directions, a rectangular strength domain is obtained for combined in-plane/out-of-plane loading. When using non-rectangular fibre-section models, this feature must be considered. Coupling with the axial load is accounted for by a fictitious axial deformation s_n assigned to the shear model. It is used only to impose the axial force equilibrium between the midheight section and the shear interface and does not correspond to any displacement of the macroelement. A non-dilatant behaviour of the shear model is assumed so that the equilibrium between the axial force acting on the interface and the axial force N_2 transferred by the midheight section can be enforced simply through Equation 8 without the need for an internal iterative scheme. The axial stiffness k_n of the shear interface is a parameter that can be chosen as an arbitrary positive number that does not need calibration, hence it is not a user input.

$$s_n = N_2/k_n. \tag{8}$$

The dependency of the shear response on the axial force N_2 also needs to be considered when assembling the basic stiffness matrix of the macroelement. Considering Equation 8 for the chain rule, when imposing axial force equilibrium between the central section and the shear interface, the derivative of the shear model with respect to the axial and flexural displacements reads:

$$\frac{\partial V_y}{\partial \boldsymbol{u_{basic,2}}} = \frac{dV_y}{ds_n}\ \frac{ds_n}{dN_2}\ \frac{\partial N_2}{\partial \boldsymbol{u_{basic,2}}}. \tag{9}$$

Such derivatives are needed when assembling the stiffness matrix of the macroelement and are condensed by the terms $\overline{\boldsymbol{k_y}}$ and $\overline{\boldsymbol{k_z}}$ relative to the shear models in local direction y and z, respectively. They can be defined as a function of the stiffness matrices $\boldsymbol{K_{int}^{(y,z)}}$ of the shear interfaces as:

$$\overline{\boldsymbol{k_y}} = \left(\frac{\partial V_y}{\partial \boldsymbol{u_{basic,2}}}\right)^T = \frac{K_{int_{2,1}}^{(y)}}{k_n} \cdot [1, 0, 0]\ \boldsymbol{K_2}. \tag{10}$$

Naming K_{tors} as the constant torsional stiffness of the element, the basic stiffness matrix is then assembled as:

$$\boldsymbol{K_{basic}} = \frac{\partial \boldsymbol{q_{basic}}}{\partial \boldsymbol{u_{basic}}} = \begin{bmatrix} [\boldsymbol{K_1}]_{3x3} & \mathbf{0} & \mathbf{0} & \mathbf{0} & \mathbf{0} & \mathbf{0} \\ \mathbf{0} & [\boldsymbol{K_2}]_{3x3} & \mathbf{0} & \mathbf{0} & \mathbf{0} & \mathbf{0} \\ \mathbf{0} & \mathbf{0} & [\boldsymbol{K_3}]_{3x3} & \mathbf{0} & \mathbf{0} & \mathbf{0} \\ \mathbf{0} & [\overline{\boldsymbol{k_y}}]_{1x3} & \mathbf{0} & K^{(y)}_{int\,2,2} & 0 & 0 \\ \mathbf{0} & [\overline{\boldsymbol{k_z}}]_{1x3} & \mathbf{0} & 0 & K^{(z)}_{int\,2,2} & 0 \\ \mathbf{0} & \mathbf{0} & \mathbf{0} & 0 & 0 & K_{tors} \end{bmatrix} \tag{11}$$

Transforming the forces and stiffness matrix from the basic to the local system is defined by the incremental compatibility and equilibrium matrices, which can include geometrical effects if the user chooses this option. The incremental compatibility matrix $\boldsymbol{\Gamma_C}$ is obtained by deriving the expressions in Equation 2 with respect to $\boldsymbol{u_{local}}$. It is computed every time the trial nodal displacements are updated if the quadratic terms in Equation 2, defining the geometric nonlinearity, are considered. If such terms are omitted, the formulation becomes linear with respect to the geometry and $\boldsymbol{\Gamma_C}$ remains constant. The inverse path, from basic forces to nodal forces, is defined by the equilibrium matrix $\boldsymbol{\Gamma_E}$. Applying the principle of contragradiency, this equilibrium matrix, which expresses the equilibrium conditions in the deformed configuration, can be obtained as in Equation 12. The complete expression defining the equilibrium matrix is reported in a supplemental document (see Section 8).

$$\boldsymbol{\Gamma_C} = \frac{\partial \boldsymbol{u_{basic}}}{\partial \boldsymbol{u_{local}}} = (\boldsymbol{\Gamma_E})^{\boldsymbol{T}}. \tag{12}$$

The equilibrium matrix can also be derived by formulating equilibrium conditions in the deformed configuration of the nodal forces. Since distributed loads acting in the direction of the element axis can induce second-order effects, their effect is included in the vector $\boldsymbol{q_0}$ and must be added to the sectional forces in the basic system. Once such forces are expressed in the local system through the incremental equilibrium matrix $\boldsymbol{\Gamma_E}$, a second vector $\boldsymbol{p_0}$, containing the reactions to the applied element loads in the local system, needs to be subtracted to ensure equilibrium at the nodes:

$$\boldsymbol{q_{local}} = \boldsymbol{\Gamma_E}\ \ (\boldsymbol{q_{basic}} + \boldsymbol{q_0}) - \boldsymbol{p_0}. \tag{13}$$

The macroelement can account for elemental forces distributed according to a rectangular or triangular profile acting along its axis; the derivation of the expressions for $\boldsymbol{q_0}$ and $\boldsymbol{p_0}$ for both cases can be found in the supplemental materials. The transformation of the stiffness matrix from the basic to the local system is slightly more involved and requires the derivation of the geometrical stiffness matrix as in Equation 14. For a linear geometry, the term $\boldsymbol{K_{geom}}$ vanishes.

$$\boldsymbol{K_{local}} = \frac{\partial \boldsymbol{q_{local}}}{\partial \boldsymbol{u_{local}}} = \frac{\partial}{\partial \boldsymbol{u_{local}}}(\boldsymbol{\Gamma_E})(\boldsymbol{q_{basic}} + \boldsymbol{q_0}) + \boldsymbol{\Gamma_E}\boldsymbol{K_{basic}}\boldsymbol{\Gamma_C}. \tag{14}$$

$$\boldsymbol{K_{local}} = \boldsymbol{K_{geom}} + \boldsymbol{\Gamma_E}\boldsymbol{K_{basic}}\boldsymbol{\Gamma_E}^{\boldsymbol{T}}. \tag{15}$$

3 | THREE-DIMENSIONAL FLEXURAL RESPONSE

Any sectional model available in OpenSees can describe the section response of the macroelement, including a fibre section of generic shape in combination with any uniaxial material model. The macroelement formulation proposed in Penna et al.[25] does not use fibre sections, instead relying on an analytically integrated section to model the flexural response. This approach is computationally efficient, so was therefore extended to biaxial bending and also implemented in OpenSees. Such a section model directly relates sectional deformations $\boldsymbol{\varepsilon_{sect}}$ (ε_0, χ_z, χ_y as defined in Figure 3) and the associated forces $\boldsymbol{q_{sect}}$ (N, M_z, M_y) of a rectangular section without numerically integrating a fibre response. This direct relationship is derived for a material with zero tensile strength, which is linearly elastic in compression until it reaches a plateau wherein damage develops. The coupled response for in-plane and out-of-plane flexure rocking is exact if no compressive damage occurs, resulting in a nonlinear elastic model; otherwise, an approximated solution can be derived whose accuracy decreases with an increasing axial load ratio.

The section response is obtained by analytical integration of the stresses in the compressed part of the section. In the reference system indicated in Figure 3, the field of axial deformations $\varepsilon(y, z)$ can be expressed as:

$$\varepsilon(y, z) = \varepsilon_0 - \chi_z y + \chi_y z = \begin{bmatrix} 1 & -y & z \end{bmatrix} \boldsymbol{\varepsilon_{sect}} = \boldsymbol{b}(y, z)^{\boldsymbol{T}} \boldsymbol{\varepsilon_{sect}}. \tag{16}$$

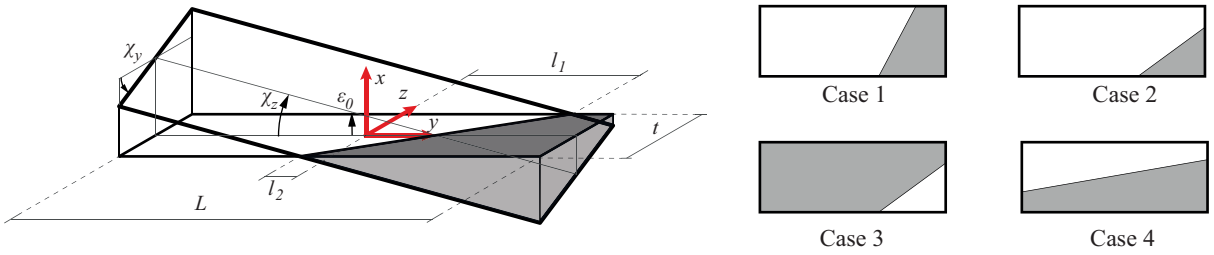

FIGURE 3 Definition of sectional reference system, variables and the cases of neutral axis orientation to be solved.

Equation 17 gives the y coordinates l_1 and l_2 of the intersection of the neutral axis with the section edge for $z = t/2$ and $z = -t/2$ (where L and t are the length and the thickness of the section, respectively). The position of the neutral axis defines the cracking condition of the section.

$$l_1 = \frac{2\varepsilon_0 + \chi_y t}{2\chi_z}, \quad l_2 = \frac{2\varepsilon_0 - \chi_y t}{2\chi_z}. \tag{17}$$

The section is fully compressed when both l_1 and l_2 are bigger than $L/2$ and the curvature χ_z is positive or, conversely, when they are both smaller than $-L/2$ and χ_z is negative. In these cases, the elastic solution given in Equation 18 applies. In the opposite case, the section is completely in tension and, according to the hypothesis of zero tensile strength, cannot transfer any force.

$$\boldsymbol{q}_{\boldsymbol{sect,el}} = \begin{bmatrix} N_{el} \\ M_{z,el} \\ M_{y,el} \end{bmatrix} = \begin{bmatrix} E\ Lt\ \varepsilon_0 \\ E\ \frac{tL^3}{12}\ \chi_z \\ E\ \frac{Lt^3}{12}\ \chi_y \end{bmatrix} \qquad \text{(elastic case)} \tag{18}$$

When the section is only partially compressed, four main cases can be defined as shown in Figure 3. The analytical solution of these cases yields a nonlinear elastic model, provided in the supplemental materials (Section 8). This represents the biaxial flexural response of the section without needing to numerically integrate a fibre section with a uniaxial constitutive model, which describes the flexural response of a rectangular section for a no-tension material in the absence of compressive damage.

Although typical axial load ratios of masonry piers are rather low, toe-crushing is often observed as a phenomenon that causes lateral failure of the element and defines its displacement capacity. Modelling the element displacement capacity in flexure as a consequence of crushing, however, requires the definition of the softening response of the material, which is neglected in the present section model. If a reliable determination of this softening response in compression is available, a fibre section in combination with an appropriate uniaxial material model can relate the displacement capacity to the material response. Alternatively, a more code-oriented approach could be adopted to define the displacement capacity of masonry elements in terms of drift limits—though these need to be applied in the in-plane direction without interacting with the out-of-plane response. Following this approach, if the displacement capacity of a flexure-controlled element is defined through a drift limit, the phenomena that the section model needs to describe for toe-crushing mainly involve reducing the lateral strength and dissipating some of the energy in loading/unloading cycles. To define the hysteretic response of a section model that does not include a numerical integration of a fibre section, the approach by Penna et al.[25] is followed. They assume a bilinear constitutive model for masonry in compression, with damage stiffness degradation, and derive correction terms applied to the section forces for in-plane bending. As an approximated solution of the problem for biaxial bending, the section can be divided into n slices (Figure 4) of width t_j, where the index y indicates the j-th slice. Their position is defined by the coordinate z_j (Equation 19). A value on the order of 5-20 is recommended for n, depending on the level of detail that is required for modelling the crushing under out-of-plane bending, as the discretisation of the section implies an approximated solution in out-of-plane bending.

$$z_j = \left(j - \frac{1}{2}\right)\frac{t}{n} - \frac{t}{2}, \qquad t_i = t_n. \tag{19}$$

$$\boldsymbol{\varepsilon}^{(j)} = \begin{bmatrix} \varepsilon_0^{(j)} \\ \chi^{(j)} \end{bmatrix} = \begin{bmatrix} \varepsilon_0 + z_j \chi_y \\ \chi_z \end{bmatrix} = \begin{bmatrix} 1 & 0 & z_j \\ 0 & 1 & 0 \end{bmatrix} \boldsymbol{\varepsilon}_{\boldsymbol{sect}}. \tag{20}$$

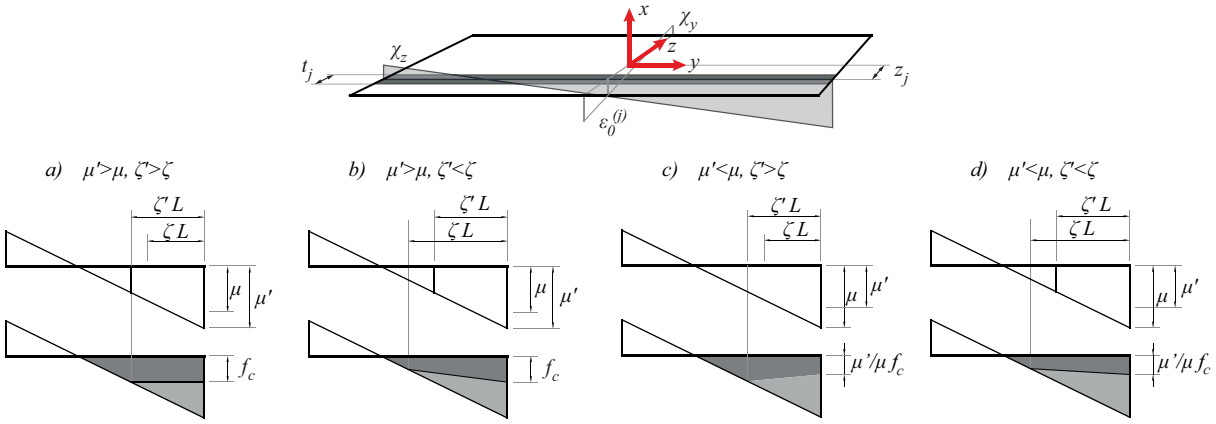

FIGURE 4 Stress distributions for four different evolutions of crushing damage variables.

The correction term $N_{c,j}$ applied to each slice follows the formulation already derived in Penna et al.[25]. It is based on two damage variables per edge, which describe the maximum ductility demand experienced by the slice edge (μ_j) and the portion of the section involved in the compressive nonlinearity (ζ_j). When a new displacement step is imposed, trial values of the damage variables (μ'_j and ζ'_j, with respect to the positive edge of the section) can be calculated from Equations 22-23. The compact notation makes use of the vectors defined in Equation 21 and is introduced only to ease the derivation of the stiffness matrix.

$$\boldsymbol{b_j} = \boldsymbol{b}\left(\tfrac{L}{2}, z_j\right) = \begin{bmatrix} 1 & -\frac{L}{2} & z_j \end{bmatrix}^T, \qquad \boldsymbol{c} = \begin{bmatrix} 0 & \frac{L}{3} & 0 \end{bmatrix}^T, \tag{21}$$

$$\mu'_j = \frac{-E\left(\varepsilon_0{}^{(j)} - \frac{L}{2}\chi^{(j)}\right)}{f_c} = -\frac{E}{f_c}\boldsymbol{b_j}^T\boldsymbol{\varepsilon_{sect}}, \tag{22}$$

$$\zeta'_j = \frac{\left(\mu'_j - 1\right)\frac{f_c}{E}}{\chi_z L} = -\frac{\boldsymbol{b_j}^T\boldsymbol{\varepsilon_{sect}} + \frac{f_c}{E}}{3\boldsymbol{c}^T\boldsymbol{\varepsilon_{sect}}}. \tag{23}$$

Depending on the previous load history, four cases are possible for each slice j, as shown in Figure 4. Each case is defined by both the relative values of the trial damage variables (μ', ζ') and the committed value of the damage variables reached in the previous load history (μ, ζ). If any current value of μ' or ζ' is bigger than the corresponding values μ or ζ, the damage parameter needs to be updated. Based on this update, the stress distributions shown in Figure 4 can be described. Cases b, c and d are approximate stress distributions that are nonlinearly distributed in the portion of the section where crushing occurs, as shown in Figure 5. The correction term $N_{c,j}$ accounting for crushing is:

$$N_{c,j} = -E\frac{\mu_j - 1}{2\mu_j}t_j\left(\zeta_j L\right)\boldsymbol{b_j}^T\boldsymbol{\varepsilon}^{(j)}. \tag{24}$$

From Equation 24, the sectional forces can be derived as:

$$\boldsymbol{q} = \boldsymbol{q_{el}} + \sum_{j=1}^{n}\begin{bmatrix} 1 \\ -\left(\frac{L}{2} - \frac{\zeta_j L}{3}\right) \\ z_j \end{bmatrix} N_{c,j} = \boldsymbol{q_{el}} + \sum_{j=1}^{n}\left(\boldsymbol{b_j} + \zeta_j\boldsymbol{c}\right)N_{c,j}. \tag{25}$$

The correction corresponding to crushing at the negative edge can be derived in the same manner. The complete expression of the correction terms that includes both edges of the section is not reported here for brevity. The tangent matrix of the sectional model can be derived from Equation 25 as:

$$\boldsymbol{K_{sect}} = \frac{\partial \boldsymbol{q_{el}}}{\partial \boldsymbol{\varepsilon}} + \sum_{j=1}^{n}\left[\left(\boldsymbol{b_j} + \zeta_j\boldsymbol{c}\right)\left(\frac{\partial N_{c,j}}{\partial \boldsymbol{\varepsilon}^{(j)}} + \frac{\partial N_{c,j}}{\partial \mu_j}\frac{\partial \mu_j}{\partial \boldsymbol{\varepsilon}^{(j)}} + \frac{\partial N_{c,j}}{\partial \zeta_j}\frac{\partial \zeta_j}{\partial \boldsymbol{\varepsilon}^{(j)}}\right)^T + \boldsymbol{c}\left(\frac{\partial \zeta_j}{\partial \boldsymbol{\varepsilon}^{(j)}}\right)^T N_{c,j}\right]. \tag{26}$$

The first term includes the derivatives of the expressions provided in the supplemental material (Section 8). The derivatives of the damage variables are obtained from Equations 22-23 when the corresponding damage variable is evolved in the current step; otherwise, they are equal to zero.

Based on this formulation, the flexural behaviour of the section under combined in-plane and out-of-plane cyclic loading can be modelled. Figure 5 shows the moment-curvature hysteresis for different orientations θ of the applied moment, ranging from pure in-plane loading ($\theta = 0°$) to pure out-of-plane loading ($\theta = 90°$). The figure is plotted for a constant axial load and a geometrical ratio $L/t = 5$. It shows that toe-crushing reduces the moment capacity and the uplift related to rocking. The consideration of toe-crushing also effects the dissipative behaviour of the section, which would be otherwise null. However, the energy dissipation related to in-plane flexural failure of masonry elements is typically much smaller than the one observed for shear failure. As an expected consequence of the simplified modelling of toe-crushing, degradation of the bending moment capacity for large curvatures is not captured by the model. Since this feature strongly affects the flexural behaviour when approaching the ultimate limit state, the complete or partial loss of lateral and/or axial force capacity must be related to a drift criterion when using such a section model, as discussed in Section 5. If a simplified treatment of local crushing phenomena is not acceptable, for the characteristics of the masonry typology of for particularly severe loading conditions, a more refined fibre section model can be applied as an alternative approach.

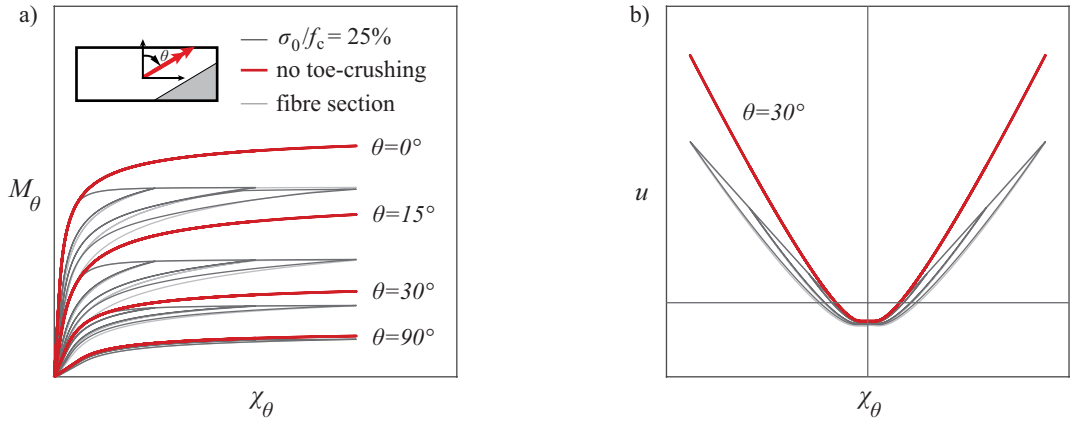

FIGURE 5 Cyclic flexural behaviour of a section for combined in-plane/out-of-plane loading using the analytical solution ($L/t = 5$, constant axial load ratio = 25%); the fibre section solution obtained for the same material model is shown as a reference. (a) Moment-curvature response for different moment orientations, with and without toe-crushing; (b) uplift of the section to orient the moment vector of $\theta = 30°$.

4 | SHEAR RESPONSE

The in-plane shear failure of a masonry panel under lateral loading can be characterised by different failure mechanisms, either (i) cracking along its diagonal in the direction of the compression strut, following only the head and bed joints or potentially also involving the tensile cracking of units or (ii) sliding along the bed joints[37]. Different failure criteria can be applied to model the two main failure mechanisms, and mainly consist of a tensile criterion, such as the one proposed by Turnšek and Čačovič[38], and a frictional criterion. However, if the diagonal cracking is approximated by a combination of sliding surfaces along the bed joints (disregarding the possible cracking of units), a frictional criterion can be applied to model both failure modes. It can be considered, moreover, that a linear failure surface in the $N - V$ plane, which describes a frictional criterion, can be obtained as a Taylor-series approximation of the parabolic failure surface that corresponds to a tensile cracking criterion[25].

As in Penna et al.[25], the macroelement models shear deformations as constant along the entire element (see Figure 1). This constant strain can be lumped into a finite displacement s of a shear spring located at the centre of the element and can be related to the shear and compression forces by a nonlinear shear model. Such a model must adequately describe the in-plane shear

response of a panel in the cyclic range, including a maximum force capacity depending on the current axial load, the stiffness reduction due to cracking before the peak force is attained, a post-peak softening response and an energy dissipation in hysteresis cycles compatible with the one observed experimentally. For this purpose, an interface model representing the macroscopic integration of a local shear criterion is needed. In this study, both the Gambarotta-Lagomarsino[39] shear model adopted in the macroelement by Penna et al.[25] as well as a different shear model corresponding to an adaptation of the cohesive/frictional interface model proposed by Alfano and Sacco[40] were implemented.

The latter model postulates that the whole surface A subjected to shear transfer can be divided into two parts, one undamaged and completely elastic A_u and a damaged A_d that is governed by a damage evolution law defining the damage parameter D and where frictional sliding occurs. Both parts are subjected to the same displacements $\boldsymbol{s} = [s_n, s]^T$.

$$A = Lt = A_u + A_d = (1 - D)A + DA. \tag{27}$$

The total forces transferred by the shear spring can be calculated as the sum of the contributions of the two parts:

$$\boldsymbol{q} = \begin{bmatrix} N \\ V \end{bmatrix} = (1 - D) \begin{bmatrix} N_u \\ V_u \end{bmatrix} + D \begin{bmatrix} N_d \\ V_d \end{bmatrix} = (1 - D)\, \boldsymbol{q_u} + D\, \boldsymbol{q_d}. \tag{28}$$

The elastic properties of the shear spring are described by Equation 29, which imposes the shear stiffness of an elastic beam with a rectangular section on the macroelement, where G is the shear modulus of masonry. The frictional sliding is represented by the inelastic displacements s_{in}. Assuming zero dilatancy, the expression in Equation 30 can be derived.

$$\boldsymbol{q_u} = \boldsymbol{K_{el}} \boldsymbol{s} = \begin{bmatrix} k_n & 0 \\ 0 & k_s \end{bmatrix} \cdot \begin{bmatrix} s_n \\ s \end{bmatrix} = \begin{bmatrix} k_n & 0 \\ 0 & \frac{5GA}{6H} \end{bmatrix} \cdot \begin{bmatrix} s_n \\ s \end{bmatrix}. \tag{29}$$

$$\boldsymbol{q_d} = \boldsymbol{K_{el}}(\boldsymbol{s} - \boldsymbol{s^{in}}) = \begin{bmatrix} k_n & 0 \\ 0 & k_s \end{bmatrix} \cdot \begin{bmatrix} s_n \\ s - s^{in} \end{bmatrix}. \tag{30}$$

If the axial force transferred by the mid-section is non-positive and the section is therefore in compression (which is always verified by the section model in Section 3), the axial strain to be applied to the shear spring can be derived as in Equation 8. On the contrary, if the axial force N_2 is positive, because of the use of a flexural section able to also transfer tension components (e.g. a fibre section model with tensile strength), it is assumed that the shear spring does not transfer any load . The plastic frictional model used is a simple Mohr-Coulomb law defined by the yield function f in Equation 31, which is a function of a constant friction coefficient μ_R and the non-associated plastic potential g.

$$f(\boldsymbol{q_d}) = \mu_R N + |V|, \qquad g(\boldsymbol{q_d}) = |V|. \tag{31}$$

Such potential enforces the zero-dilatancy hypothesis, since:

$$\boldsymbol{s^{in}} = \dot{\lambda} \frac{\partial g}{\partial \boldsymbol{q_d}} = \dot{\lambda} \begin{bmatrix} 0 \\ \text{sign}(V) \end{bmatrix}. \tag{32}$$

Loading-unloading conditions are defined by the usual Kuhn-Tucker conditions, i.e.:

$$\dot{\lambda} \geq 0, \qquad f(\boldsymbol{q_d}) \leq 0, \qquad \dot{\lambda}\, f(\boldsymbol{q_d}) = 0. \tag{33}$$

The solution of a finite displacement increment does not require any iterations if the friction coefficient μ_R is constant. A trial state corresponding to a purely elastic increment can be defined as:

$$\boldsymbol{q_d}^{trial} = \boldsymbol{K_{el}}(\boldsymbol{s} - \boldsymbol{s_n^{in}}). \tag{34}$$

If the trial value of the yield function is positive in the trial state defined by Equation 34, the increment of the plastic multiplier $\Delta\lambda$ is calculated as:

$$\Delta\lambda = \frac{\mu_R N^{trial} + |V^{trial}|}{k_s}. \tag{35}$$

The damage evolution law, which controls the evolution of the damaged portion of the surface subjected to shear, has to account for all the phenomena that cause a reduction of the force capacity and stiffness of a masonry element failing in shear. If the local

response is modelled, a common hypothesis assumes that only the cohesive contribution undergoes damage[40,39]. However, when modelling the element response of a masonry wall, the cohesion and friction angle are typically derived by fitting a linear trend to the force capacity measured in experimental tests[41]. In this case, assuming that damage is only associated with cohesion can result in an insufficient reduction of the force capacity in the post-peak range and an excessive energy dissipation in hysteresis cycles. To overcome this, the damage law originally used by Alfano and Sacco[40] is modified with the assumption that part of the frictional contribution can be lost in the damage process. In such a model, the maximum force capacity is controlled by a friction coefficient μ_0, which can be derived directly from experimental test series or code values. Additionally, the parameter μ_R can be tuned to better match the post-peak response and energy dissipation, and it controls the frictional law in Equations 31-35. The residual force capacity is $\mu_R N$, and the total loss in force therefore corresponds to the cohesive contribution and part of the frictional contribution equal to $(\mu_0 - \mu_R)N$.

The progressive force capacity loss is controlled by the damage law, which is defined as a function of the total interface displacements s, to obtain a phenomenological model that reproduces the main features of the cyclic response of a masonry wall. The pre-peak response is defined by a maximum force capacity V_{max} reached for a certain displacement s_{max}. As in Penna et al.[25], s_{max} is written as a function of a parameter G_c, which controls the stiffness reduction after damage initiation (Figure 6a). The force capacity can, in principle, be defined by any criterion depending on the axial force N, provided that it is bigger than the residual shear strength for any possible value of N. For this study, the Mohr-Coulomb criterion in Equation 36 is applied, which satisfies this condition for all $\mu_0 \geq \mu_R$.

$$V_{max} = cLt - \mu_0 N. \tag{36}$$

This linear criterion can also be interpreted as a linearisation of different failure criteria[25], such as the criterion proposed by Mann and Muller[42] or Turnšek and Čačovič[38], around the expected axial load. The displacement s_{max} can be defined as a function of the displacement s_0, which corresponds to the attainment of the maximum frictional contribution; after this point, damage evolves, and the displacement associated with the damage contribution can be calculated as:

$$s_{max} = \frac{-\mu_R N}{k_s} + (1 + G_c)\frac{V_{max} + \mu_R N}{k_s} = s_0 + (1 + G_c)s_{el}. \tag{37}$$

An adimensional parameter x can then be defined as:

$$x = \frac{k_s|s| + \mu_R N}{k_s s_{max} + \mu_R N}. \tag{38}$$

When $x \leq 1$, the element is in the pre-peak part of its response, and the damage evolution law is expressed by Equation 39, which ensures that the peak force is attained for a displacement s_{max} with zero tangent stiffness.

$$D = \left(1 - \frac{1}{1 + G_c}\right) x^{\frac{1}{G_c}}, \qquad \text{for } x \leq 1. \tag{39}$$

The post-peak response is characterised by a progressive reduction of the force capacity, which is imposed as linear by the present model. The post-peak stiffness k_{pp} (assumed positive for a softening response) can be expressed as a function of the displacement s_ξ, for which a force drop of ξV_{max} is attained:

$$k_{pp} = \frac{\xi V_{max}}{s_\xi - s_{max}}. \tag{40}$$

Setting $\xi = 0.2$ defines the post-peak response as a function of the displacement corresponding to a 20% force drop. This displacement, expressed in terms of drift, is often considered when defining the ultimate limit state of a masonry wall and can be derived from either experimental results or code provisions. Imposing a linear decrease of the force capacity in the post-peak range, the second branch of the damage law can then be defined as:

$$D = \frac{1}{k_s|s| + \mu_R N}\left[\left(k_s + k_{pp}\right)|s| - \frac{k_{pp}}{k_s}G_c\mu_R N - \frac{k_{pp}}{k_s}(1 + G_c)V_{max} - V_{max}\right] \leq 1, \qquad \text{for } x > 1. \tag{41}$$

The algorithmic tangent operator can be obtained as in Alfano and Sacco[40] by computing the derivatives of the damage evolution law with respect to the interface displacements. Such derivatives, omitted here for brevity, can be obtained directly

from Equations 39-41 when damage evolution occurs, applying the condition in Equation 8 for axial equilibrium and the chain rule. If there is sliding, and therefore $\Delta\lambda > 0$, the matrix $\boldsymbol{H_t}$ can be obtained from Equation 43; in all other cases, $\boldsymbol{H_t} = \boldsymbol{K_{el}}$.

$$\boldsymbol{K_{int}} = (1 - D)\boldsymbol{K_{el}} + D\boldsymbol{H_t} - \boldsymbol{K_{el}}\boldsymbol{s}\left(\frac{\partial D}{\partial \boldsymbol{s}}\right)^T + \boldsymbol{q_d}^{trial}\left(\frac{\partial D}{\partial \boldsymbol{s}}\right)^T. \tag{42}$$

$$\boldsymbol{H_t} = \begin{bmatrix} k_n & 0 \\ -\text{sign}(V)\mu_R k_n & 0 \end{bmatrix}, \qquad \Delta\lambda > 0. \tag{43}$$

The influence of the model parameters on the envelope of the shear response is shown in Figure 6a. The behaviour enters the nonlinear range when the shear force exceeds the residual frictional contribution $\mu_R N$. The maximum force is reached for a displacement determined by the parameter G_c, which controls the softening of the response after nonlinearity occurs; for a value of $G_c = 1$, the response is linear up to the maximum capacity. The linear post-peak branch is determined by specifying the drift at which a 20% force drop is reached. When damage evolution is completed, the residual force capacity $\mu_R N$ is retained. The cyclic response is governed mainly by the choice of μ_R, which controls both the residual force capacity and the shape of the hysteresis cycles. The introduction of the residual friction coefficient μ_R therefore allows imposing different hysteretic responses without altering the peak force capacity (Figure 6b).

As an alternative to the model presented in Equations 27-43, the shear model proposed by Gambarotta and Lagomarsino[39] and implemented in the research version of the software Tremuri[25] was implemented in OpenSees and can be used in combination with the proposed macroelement. Such a model also describes the cyclic shear response as a combination of a frictional contribution and a cohesive contribution. Only the cohesive contribution undergoes damage, as one obtains with the model in Equations 27-43 if $\mu_R = \mu_0$. Details on the implementation are given in Penna et al.[25], to which only the derivation of the tangent operator was added to allow for quadratic convergence in global iterations. If the user wishes to decouple the shear response from the axial load, any uniaxial material law implemented in OpenSees can describe the shear response.

The application of the model in Equations 27-43 to three shear-compression cyclic experimental tests on stone masonry walls is shown in Figure 7. The experimental curves were derived in a test campaign[43] on six single-leaf stone masonry walls. The walls, of dimensions 0.90 x 0.90 x 0.20 m, were built with a regular masonry texture made of squared limestone blocks and hydraulic lime mortar (for a comprehensive description of the test campaign refer to Godio et al.[43]). All walls were tested under fixed-fixed boundary conditions, imposing a constant shear span equal to half of the wall height. Different loading histories were applied ranging from monotonic to cyclic with 2 or 100 repeated cycles per drift level. Only cyclic tests with two repeated cycles per drift level were extracted, as they are generally the most representative of the seismic demand imposed on masonry walls in regions of low to moderate seismicity. Figure 7 compares the experimental results and numerical simulations for walls SC1, SC5 and SC4, which were tested under an axial load ratio of 7.5%, 11.25% and 15%, respectively, and all failed in shear. The macroelement parameters applied to all three tests are given in Table 1 . The elastic modulus E and the compressive strength f_c are derived from two compression tests on masonry wallettes. The shear modulus G is assumed to be equal to $E/3$. The

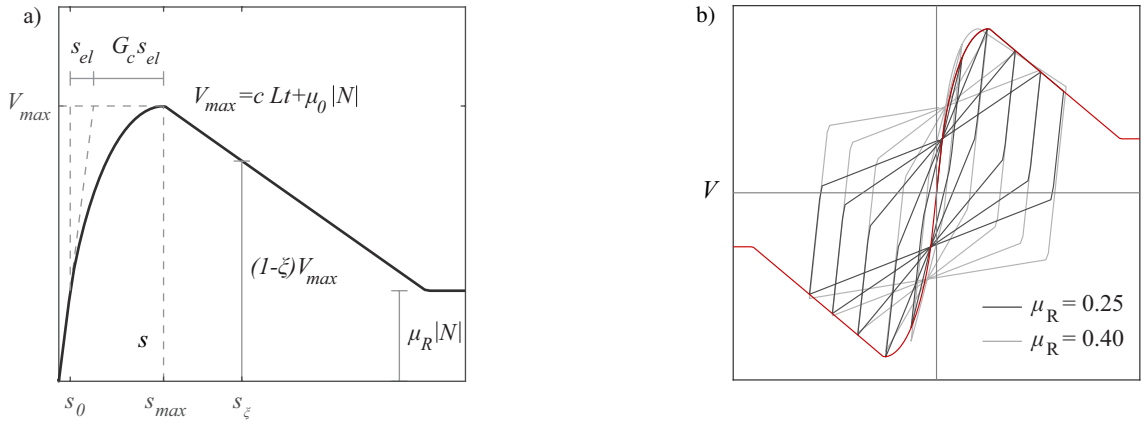

FIGURE 6 (a) Parameters defining the envelope of the shear response ($G_c = 3$, $\mu_0 = 0.40$, $\mu_R = 0.25$, $\xi = 0.20$). (b) Influence of the residual friction coefficient μ_R on the cyclic shear response.

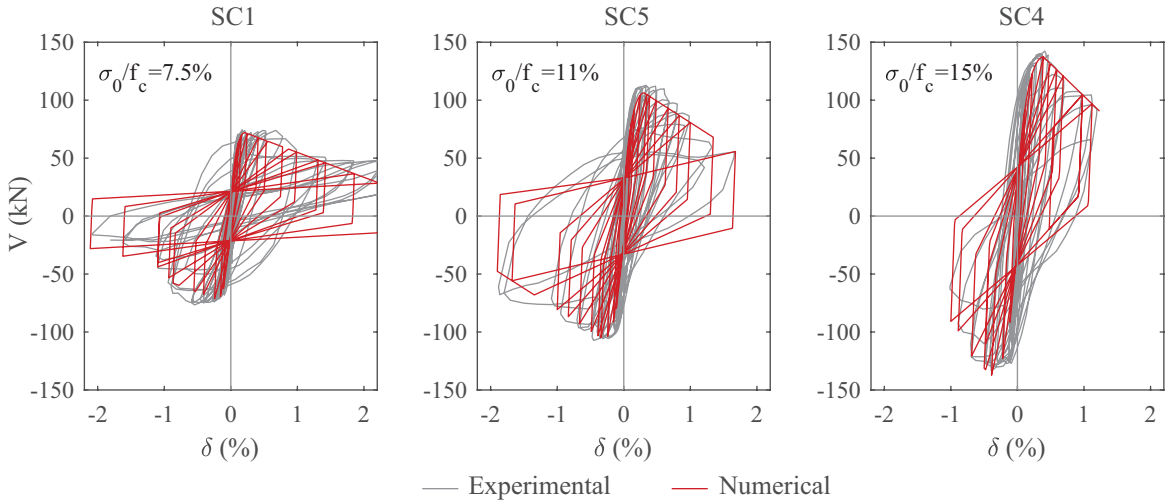

FIGURE 7 Comparison between numerical and experimental[43] cyclic shear responses under three different axial load ratios.

cohesion c and the friction coefficient μ_0 are derived from linear regression of the maximum shear capacities of all six tested walls[43]. The drift at 20% capacity drop δ_u is derived as the average of the the drift capacities of walls SC5 and SC4, considering both the positive and negative envelopes. The residual friction coefficient μ_R is assumed to be equal to $\mu_0/3$. When imposing the same displacement histories as applied in the physical tests, the macroelement captures the envelope and some of the features of the cyclic response of the tested walls. In particular, the possibility of defining an initial friction coefficient, controlling the maximum force capacity, different from the residual friction coefficient, which mainly controlling the dissipative hysteretic behaviour, uncouples the fitting of the envelope curve under different axial loads from the fitting of a proper hysteretic energy dissipation. The asymmetry of the numerical response of the walls depends only on the asymmetry of the imposed displacement history, since the applied shear model would not define any asymmetric behaviour under a symmetric displacement history.

TABLE 1 Material properties used in the numerical simulations of the three tests SC1, SC5 and SC4[43].

E [MPa]	G [MPa]	f_c [MPa]	c [MPa]	μ_0	μ_R	G_c	δ_u [%]
4200	1400	10.0	0.05	0.47	0.16(*)	6.0(*)	0.87

(*) Calibrated parameter; all remaining values provided in Godio et al.[43]

5 | IN-PLANE DISPLACEMENT CAPACITY

Masonry buildings are often highly redundant structures, so assuming that such buildings fail when the first element fails would be very conservative. For this reason, a modelling approach that captures the progressive strength loss and force redistribution to other members is often necessary. A masonry pier subjected to in-plane loading first loses its horizontal and then ultimately its axial load bearing capacity. Therefore, the macroelement is formulated such that both the horizontal and axial load bearing loss can be simulated.

Because of their formulations, the sectional models used for the flexural and the shear response of the macroelement may not properly simulate the loss of lateral strength of existing masonry walls. The shear model presented in Section 4 describes a strength decrease in the post-peak range and a residual strength contribution, but once the residual strength $\mu_R N$ is reached, the strength does not degrade further. The sectional model proposed for the flexural response in Section 3 does not explicitly describe a maximum displacement capacity nor a loss of axial load bearing capacity. Although more complex sectional models

could explicitly capture both features, such as through the use of a fibre section and a material law modelling a softening response during crushing, the new macroelement instead offers the possibility to specify drift limits at the element level in which first the horizontal and then the axial load bearing capacity are lost.

The in-plane shear and flexural drift components of the element in a deformed configuration are extracted from the basic displacements defined in Equation 2, removing rigid-body rotations, as:

$$\delta_{SH} = \frac{|s_y|}{H}, \tag{44}$$

$$\delta_{FL} = \max\left[\left|\varphi_{z1} + \frac{\varphi_{z2}}{2}\right|, \left|\varphi_{z3} + \frac{\varphi_{z2}}{2}\right|\right]. \tag{45}$$

Only in-plane displacement component are accounted for when defining the drift demand on the element. Although an interaction between the in-plane and out-of-plane response is captured as a concentration of compressive stresses at the section level, the influence of combined in-plane and out-of-plane loading is not included in the displacement capacity model, due to the scarcity of experimental evidence on the phenomenon. Drift models for in-plane loading derived from collections of experimental shear-compression tests on masonry walls trend towards a decrease in lateral drift capacity with an increasing axial load ratio, despite the high uncertainty related to the estimation of the drift capacity, both for modern unreinforced brick masonry[44,45,46] and for stone masonry walls[41]. To account for such trend, two generic drift models—one for shear and one for flexural failure—can be defined as a function of the applied axial load ratio $\frac{\sigma_0}{f_c}$ and the shear span H_0. These models can be expressed in a generic form as:

$$\delta_{SH,HC} = f_1\left(\frac{\sigma_0}{f_c}\right) \cdot \left(\frac{H_0}{H}\right)^{\beta}, \quad \delta_{FL,HC} = f_2\left(\frac{\sigma_0}{f_c}\right) \cdot \left(\frac{H_0}{H}\right)^{\beta}, \tag{46}$$

in which f_1 and f_2 are user-defined functions of the axial load ratio and the coefficient β. They can represent a piecewise linear drift model[45,41], or, more simply, a constant drift capacity that disregards any effect of the axial load ratio, as indicated by the current version of Eurocode 8[47]. When exceeding the drift capacity specified by Equation 46, the lateral force capacity of the macroelement is either set to zero or reduced by a user-specified factor. At this point, the axial load bearing capacity is still maintained and is cancelled only when the drifts specified by Equation 46 are exceeded by a factor $\alpha_{\frac{AC}{HC}}$.

$$\delta_{AC} = \alpha_{\frac{AC}{HC}} \cdot \delta_{HC}. \tag{47}$$

After attaining the drift limit corresponding to axial load collapse δ_{AC} defined in Equation 47, the element capacity in the axial and lateral directions is cancelled or reduced by a user-defined factor.

6 | OUT-OF-PLANE BEHAVIOUR

The out-of-plane response of unreinforced masonry walls includes a first phase in which the wall deforms and cracks. In a second phase, a rocking mechanism develops until the stability point of the wall is reached, wherein the wall cannot resist any out-of-plane action. The problem can be analysed by considering the masonry elements as an assembly of rigid[48,27] or deformable blocks[49,50,51].

When performing dynamic analyses of out-of-plane loaded masonry walls, it is essential to capture the force-displacement behaviour over the entire range of displacements. This is because an element subjected to out-of-plane rocking can resist significantly larger lateral accelerations before overturning than those that lead to the initiation of the rocking mechanism[49]. The first part of the out-of-plane response of the new macroelement is governed by the chosen sectional model, while the second part of the response is controlled by the stability mechanisms described by the $P-\Delta$ formulation. In the following, the behaviour of the macroelement under static out-of-plane loading is compared to limit analysis results (Section 6.1). Then, the dynamic behaviour, which depends on the static force-displacement curve as well as on the chosen mass discretisation and damping model, is compared to analytical solutions and experimental results (Section 6.2).

6.1 | Static Out-Of-Plane Response

The force-displacement behaviour of a single macroelement under uniform out-of-plane loading is compared to the limit response of rigid block models in Figure 8. The analyses are performed for three different boundary conditions. The rigid block

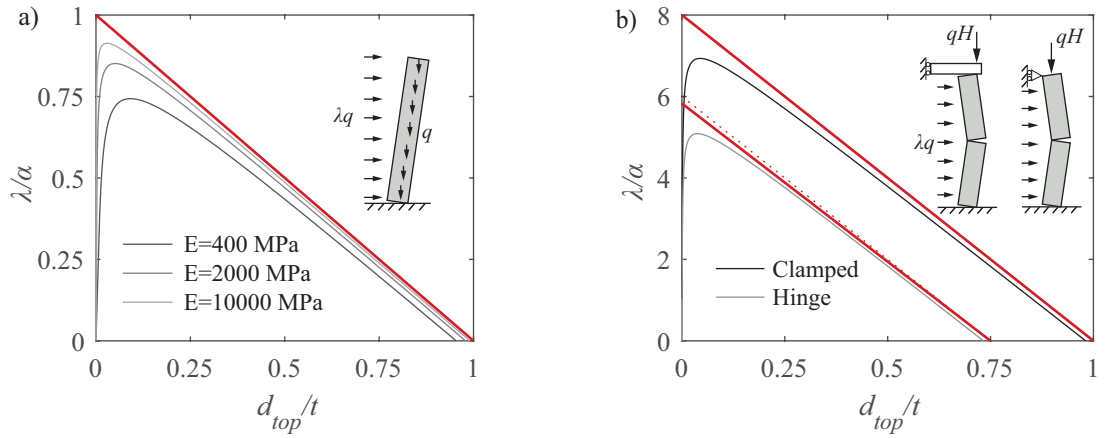

FIGURE 8 Comparison of the out-of-plane response of one macroelement with rigid body solutions ($H = 1.1$ m, $t = 0.22$ m, $\alpha = H/t = 5$, $G/E = 0.35$, $f_c = 3.0$ MPa, $q = 22$ kN/m^3): (a) cantilever element under distributed loads; (b) simply supported wall spanning floors for different boundary conditions, subjected to overweight and distributed lateral load, for E=2000 MPa.

response (red line in Figure 8) is defined by a limit load multiplier λ_0 and a stability point at which the horizontal force drops to zero. For comparison, a sectional model was chosen that reflects the hypotheses of the limit analysis of rocking blocks (zero tensile strength, infinite compressive strength, very high axial stiffness), and therefore, the two analyses provide similar results. The reduction in the force capacity with a reduction in stiffness of the macroelement is in line with the results of analytical models[51].

The macroelement solution provides the same results as the rigid block analysis for a cantilever wall (Figure 8a) and a wall with clamped-clamped boundary conditions (Figure 8b, case "Clamped"). When the wall is clamped at the bottom but the rotations at the top are unrestrained (Figure 8b, case "Hinge"), the minimum load multiplier obtained though limit analysis corresponds to a mechanism with a middle hinge slightly above mid-span, though the formulation of the macroelement assumes that the third hinge is always at midheight, which introduces a small error. Regardless, the rigid block solution, which corresponds to a hinge location at mid-span (dotted line in Figure 8b), is rather close to the exact solution that places the hinge above midheight. This agrees with the findings by Derakhshan et al.[52], who stated that locating the hinge at mid-span is typically acceptable, since the theoretical position of the hinge is not very different for most overburden to self-weight ratios. Rotations may be restrained, for example, by slabs with considerable out-of-plane bending stiffness or ring beams. For very flexible floors, which is common for historical buildings, the rotation at the wall top is generally not significantly restrained.

6.2 | Dynamic Out-Of-Plane Response

The dynamic out-of-plane response of the macroelement is governed both by the quasi-static capacity curve as well as the chosen mass distribution along the element and the applied damping model. A consistent mass matrix was derived that accounted for all deformation modes and a uniformly distributed mass along the element axis. As a numerically simpler alternative, the approximated diagonal lumped mass matrix can also be used. The consistent mass matrix leads to an improved modelling of inertial properties when compared to a diagonal lumped mass matrix, though has a slightly increased numerical cost. For implicit analyses, this increase is often marginal, though for some explicit analyses, the use of a diagonal mass matrix can provide a significant cost reduction. The derivation of both consistent and lumped mass matrices, and the error related to the latter, are reported in the supplemental materials (Section 8). Both mass matrices have been implemented for the macroelement in OpenSees, and the user can chose between the two; all results presented in the following are obtained with a consistent mass matrix formulation.

An additional aspect governing the out-of-plane dynamic response of the macroelement is the damping model that accounts for energy dissipation in rocking oscillations. The macroelement can model dissipative phenomena both at the level of the sectional response and through viscous damping and/or numerical damping. However, because significant crushing at the section edge does not take place for moderate axial loads, the dissipative behaviour under rocking oscillations is related mainly to damping. Since the first analytical studies on rigid blocks[53], the dissipative phenomena of a rocking block are assumed to take

place primarily at each impact. This energy dissipation is described by a coefficient of restitution relating the angular velocities before and after impact. Using this approach, the free oscillation motion of a rigid rocking block is described by the following equation[54]:

$$I_O\ddot{\theta} - mgR\sin\left(\alpha \operatorname{sign}\theta - \theta\right) = 0, \tag{48}$$

where α is equal to atan(H/t), m is the mass of the block and $R^2 = H^2 + t^2$ (see Figure 9). To define the coefficient of restitution, one criterion that can be applied is the conservation of the angular momentum at the instant of an impact. As derived by Housner[53], the ratio e between the angular velocity before the impact $\dot{\theta}_1$ and after the impact $\dot{\theta}_2$ can be expressed, in this case, as:

$$e = \frac{\dot{\theta}_2}{\dot{\theta}_1} = 1 - \frac{3}{2}\sin^2\alpha. \tag{49}$$

However, the energy dissipation of finite element tools that are used in structural engineering is commonly treated through viscous models. Although a rocking block and an elastic oscillator are fundamentally different[54], a numerical simulation with common finite element solvers needs an approximation of the instantaneous energy dissipation of a rigid body at impacts with an equivalent damping model. A possible approach is to rely only on numerical damping, which can be done if a dissipative integration scheme is applied, as proposed by Vassiliou et al.[55]. If the element is used in a larger structural model that includes elements that are mainly loaded in-plane and elements with a principal out-of-plane response at the same time, however, the use of a classical Rayleigh damping can be preferable. In this case, the modelling of the energy dissipation must be achieved through an appropriate viscous damping model. Inserting a velocity-proportional term in the inverted pendulum equation gives:

$$I_O\ddot{\theta} + c\dot{\theta} - mgR\sin\left(\alpha \operatorname{sign}\theta - \theta\right) = 0. \tag{50}$$

A calibration of the viscous damping c, which produces an energy dissipation comparable to that of Housner's model in Equation 48 for fairly large rotation angles θ, was proposed by Vassiliou et al.[56] as:

$$c(\alpha, m, R) = c_0 = 0.02\left(\frac{\alpha}{0.1}\right)^2 mg^{0.5}R^{1.5}. \tag{51}$$

If a stiffness-proportional Rayleigh damping model is applied to the macroelement, wherein the damping matrix $\boldsymbol{C}$ is set equal to $\beta_K \boldsymbol{K}$, an equivalent expression for β_K is needed. Considering an initial-stiffness-proportional model, for an idealised element rotation θ as a rigid block, one can assume that only the base section of the macroelement deforms and that the rotation takes place exactly around the edge of the section. In this case, Rayleigh damping forces can be written as:

$$\boldsymbol{C^{(1)}\dot{u}^{(1)}} = \beta_K \boldsymbol{K_{in}^{(1)}\dot{u}^{(1)}} = \beta_K \frac{1}{\overline{w_1}H}\begin{bmatrix} EA & 0 & 0 \\ 0 & EI_z & 0 \\ 0 & 0 & EI_y \end{bmatrix}\begin{bmatrix} t/2 \\ 0 \\ 1 \end{bmatrix}\dot{\theta}. \tag{52}$$

It can then be imposed that the moment around point O resulting from the stiffness-proportional damping forces is equal to the viscous damping moment, which yields Equation 53. For a rectangular section, Equation 54 gives an explicit expression for the Rayleigh coefficent β_K.

$$M_O = \frac{\beta_K}{\overline{w_1}H}\left(EA\frac{t^2}{4} + EI_z\right)\dot{\theta} = c_0\,\dot{\theta}, \tag{53}$$

$$\beta_K = c_0\,\frac{\overline{w_1}H}{4I_y}. \tag{54}$$

It is known that the use of initial-stiffness-proportional Rayleigh damping can be problematic for strongly nonlinear systems[57,58]. Initial-stiffness-proportional damping, however, is preferred here over tangent stiffness-proportional damping both to avoid negative damping due to the negative terms in the stiffness matrix related to nonlinear geometry effects and to avoid abrupt changes of damping forces at each impact, which would introduce numerical damping and an excessive time-step dependency of the solution. Moreover, calibrating the damping coefficient according to Equations 51-54 mitigates the problem of unrealistically high damping forces[58] that often occur when initial-stiffness-proportional damping is used. The possibility of using the same damping model, for both in-plane loaded and out-of-plane loaded elements, however, remains an open theme.

Numerical solutions of the differential equations in Equations 48 and 50 and the response of a single macroelement subjected to free vibrations are compared in Figure 9a. The equivalent damping ratio of the macroelement is calculated from the free-vibration response with the logarithmic decrement method, assuming a damping ratio $\xi \ll 1$ and comparing maximum rotation amplitudes at the beginning and at the end of each complete rocking cycle, i.e. between two consecutive impacts at the base. Figure 9b plots the equivalent viscous damping ratios. The energy dissipation of the macroelement model, evaluated in terms of equivalent damping ratio, agrees rather well with Housner's solution, particularly for larger rotations. The results were obtained for a stiff block ($E = 50$ GPa) of dimensions 1.10 x 0.22 m using a consistent mass matrix formulation and neglecting the inertial contributions in the axial direction to avoid modelling vertical vibrations at impacts. Results can also be compared to the simplified expression given in Makris and Konstantinidis[54] (Equation 55), which yields a constant equivalent viscous damping equal to 4% for any θ to α ratio for the considered case.

$$\xi = -0.34 \ln e^2. \tag{55}$$

Derived by Housner under the hypothesis of conservation of angular momentum, the coefficient of restitution is a reference solution that provides a theoretical framework defining a reasonable range for the energy dissipation related to the rocking motion and highlighting the main parameter governing the phenomenon, i.e. the slenderness of the rocking block. This dependency is generally confirmed by experimental results, which show a higher energy dissipation for stockier blocks[59]. However, an exact experimental confirmation of Housner's hypothesis is lacking, particularly for materials such as masonry that do not perfectly respect the hypotheses of the theoretical model. For example, tests on the two-way rocking of masonry parapets[60,61] tend to show a higher energy dissipation. Sorrentino et al.[60] found that experimentally derived coefficients of restitution are approximately 5-8% lower than theoretical coefficients. Although the difference appears to be small, the effect on the experimental displacement histories, and therefore on the equivalent damping ratio, is considerable. The effects of the block stiffness and interface conditions are studied in detail in ElGawady et al.[62], who also found a non-negligible increase in energy dissipation for blocks rocking under imperfect conditions. On the other hand, when the stiffness of the material and the characteristics of the rocking surface approach the ideal conditions of the model, such as for the granite tested by Peña and Lourenço[59], the experimental results are closer to the theoretical solution.

When modelling the out-of-plane response of a masonry wall through a single macroelement, an experimental energy dissipation larger than the one corresponding to Housner's model can be either captured by calibrating the viscous damping or by explicitly modelling the finite stiffness of the block and the possible crushing at the interface. For reference experimental results, a free-vibration out-of-plane test on an irregular stone masonry cantilever wall, carried out by Degli Abbati and Lagomarsino[61], is used here. In this campaign, three-leaf stone masonry walls built with lime mortar were tested by imposing an initial out-of-plane displacement, which was subsequently released to perform a free-vibration test. Each wall was subjected to several free-vibration tests. From the test series, which comprises three walls, "panel 1" (dimensions 1.10 x 0.90 x 0.22 m) is

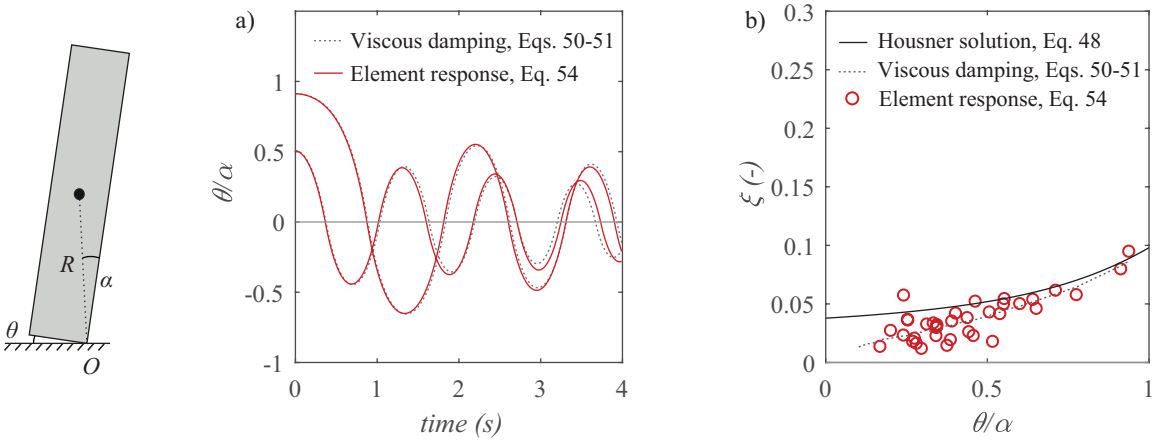

FIGURE 9 Rigid block theoretical solution and numerical response of free vibrations of a single block: (a) displacement history (b) and equivalent viscous damping ratio.

the most regular in terms of physical hinge location and the slenderness ratio, and it is modelled through a single macroelement. Experimental results are compared to the numerical displacement time histories and equivalent damping ratio (Figure 10).

The dissipative behaviour of the experimental sample is markedly higher than the ideal sample shown in Figure 9 for a rigid block of the same dimensions. The increased damping, as discussed in Degli Abbati and Lagomarsino[61], can be related to the sum of three phenomena, i.e. the progressive detachment from the base when the centre of rotation switches from one edge to the other at impact, the elastic deformability of the panel and the inelastic deformations at the toe. Although such features are accounted for by the macroelement model, an increased viscous damping must be specified to capture the correct energy dissipation. A factor of 6 is found between the damping coefficient derived in Equation 54 and the damping coefficient that best matches these experimental results over all θ to α ratios. The viscous damping model, compared to Housner's model, tends to underestimate the energy dissipation for smaller rocking amplitudes (see Figure 9b). However, experimental results follow a similar trend, showing a smaller energy dissipation than the one postulated by Housners's model for low amplitude oscillations (Figure 10b).

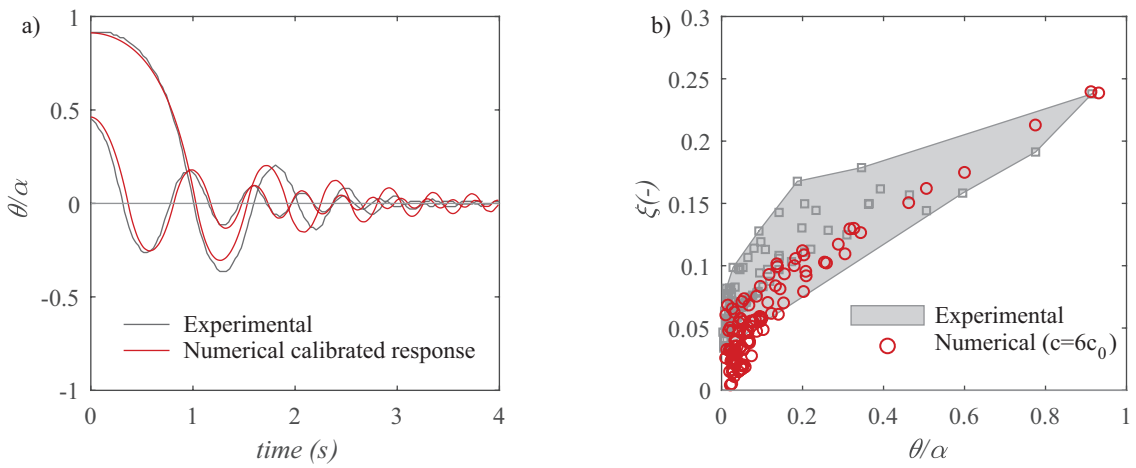

FIGURE 10 Comparison of experimental (digitised from Degli Abbati et al.[63]) and numerical responses of a single element: (a) displacement history (b) and equivalent damping ratio.

7 | CONCLUSIONS

Herein, a novel macroelement formulation for modelling masonry structures by means of equivalent frame models was developed and implemented in the open-source software OpenSees. The in-plane response of the macroelement builds on the macroelement by Penna et al.[25], and has been enhanced to additionally capture the out-of-plane response of the masonry element. The macroelement can be used to model the nonlinear behaviour of a pier, spandrel or gable wall (for the latter, a mass matrix accounting for the triangular shape has been derived) with a single element .

The presented macroelement is defined by the degrees of freedom of three nodes, two end nodes and a node at midspan, in three-dimensional space. The degrees of freedom describe the kinematics of two blocks, which are deformable in shear and are bounded by three interfaces that capture the axial and flexural deformations. The macroelement can account for second-order geometric effects through a $P-\Delta$ formulation. It can also exactly reproduce, in the elastic regime, the displacements at the extremities of a three-dimensional Timoshenko beam subjected to forces concentrated at the end nodes and with linearly distributed loads. In the nonlinear range, it ensures the exact application of equilibrium conditions at three flexural interfaces. This macroelement therefore couples the flexural behaviour as well as the shear behaviour with the axial load without nested internal iterations.

If the element is used to simulate the in-plane and out-of-plane response of a masonry wall, adequate sectional models need to be applied. Any sectional model available in OpenSees can be used for the macroelement. For the flexural response, fibre sections with suitable constitutive laws for the fibres can be used. As an alternative, an analytical sectional model describing three-dimensional rocking, accounting for zero tensile strength and toe-crushing, is proposed in this study. Developed with the objective of reducing the computational cost of the analysis, which is a key feature for applications in dynamic analyses of equivalent frame models, it can capture the main features of the in-plane and out-of-plane flexural response. For shear, a model based on the damage model and friction interface model by Alfano and Sacco[40] was developed, which couples the shear behaviour to the axial load. The results of the macroelement are fairly similar to experimental results in terms of the force-displacement envelope and hysteretic energy dissipation. The in-plane behaviour of the macroelement, when coupled with the proposed sectional models, agrees with both well-established formulations for the force capacity of masonry walls and with numerical simulations obtained through the software Tremuri[14,25], whose shear model is also implemented, as an alternative given to the user. The interaction between the shear and axial response is introduced as a direct dependency between the shear force capacity and the axial load. When relevant compressive softening phenomena are present, and mixed failure modes occur, such interaction model can be rather simplified. In this case in particular, a calibration based on a set of experimental evidences is necessary.

The possibility of including both the in-plane and out-of-plane response of a masonry wall in the macroelement opens up the potential of using one equivalent frame model to assess, through dynamic time-history analyses, both types of failure. The macroelement is shown to replicate the rigid block limit analyses of one-way bending out-of-plane mechanisms. When the out-of-plane failure mode to be predicted is more complex, the response may be only approximated by the interaction between elements, as would occur, for example, at the corners of a building, if openings are present. However, for complex, two-way bending failure modes, a beam idealisation for the response of a masonry wall is not sufficient and more refined approaches are needed. In dynamic analyses, the macroelement response depends strongly on the applied damping model, for which a possible approach using initial-stiffness-proportional damping is proposed; the theoretical solutions from this approach were in good agreement with the experimental results. The application of such a damping model in a more complex structure, including where both elements are loaded in-plane and out-of-plane, however, remains a topic for future research.

Despite their simplicity, equivalent frame models, applied in conjunction with dynamic simulations, can provide useful insights regarding the seismic behaviour of masonry buildings for a moderate numerical cost. As a result, they are well suited to investigate the effect of aleatoric and epistemic uncertainties on the building response. In this spirit, the macroelement implemented in OpenSees allows the user to choose between several options regarding (i) the mass matrix (consistent vs lumped mass matrix), (ii) shear models (two models were implemented for the macroelement; additionally, any user-defined biaxial constitutive model, or, if the user wishes to decouple the shear response from the axial load, uniaxial constitutive model, can be used), (iii) damping models (initial-stiffness-proportional vs tangent-stiffness-proportional models), (iv) drift capacity models for the in-plane response, which can depend on the failure mode and/or the axial load ratio. Furthermore, the macroelement offers the choice to reduce both the horizontal stiffness and strength when a certain drift limit is reached as well as the axial load-bearing capacity. The drift at which the axial load-bearing capacity is cancelled or reduced is given by a user-defined factor multiplied by the drift at horizontal load failure.

In addition to the modelling choices linked to the macroelement, the user can profit from all the possibilities of a complex finite element software, in terms of nonlinear material models, element types and sectional models, when modelling a masonry building using OpenSees. The new macroelement can therefore also be used to investigate the performance of mixed structures or retrofitted structures, and, through the use of fibre sections coupled with adequate material models, might be applied for better describing the behaviour of spandrels.

8 | REPOSITORY

The code of the element can be downloaded from https://github.com/eesd-epfl/OpenSees/wiki. The repository contains, next to the element implementation, an OpenSees library including the element. Furthermore, the repository shares examples used to produce the figures in this manuscript, and a supplemental document including the derivations omitted here for brevity (https://github.com/eesd-epfl/OpenSees/wiki/Supplemental-materials).

9 | ACKNOWLEDGEMENTS

This work was prepared as part of the Basel-Project, which is supported by the Swiss Federal Office of the Environment and the Construction Department of the Canton Basel-Stadt.

References

1. Zhang S., Mousavi S. M. T., Richart N., Molinari J.-F., Beyer K.. Micro-mechanical finite element modeling of diagonal compression test for historical stone masonry structure. *International Journal of Solids and Structures.* 2017;112:122–132.

2. Lourenço P. B., Rots J. G.. Multisurface interface model for analysis of masonry structures. *Journal of Engineering Mechanics.* 1997;123(7).

3. Wilding B. V., Dolatshahi K. M, Beyer K.. Influence of load history on the force-displacement response of in-plane loaded unreinforced masonry walls. *Engineering Structures.* 2017;152:671–682.

4. Milani G., Lourenço P. B., Tralli A.. 3D homogenized limit analysis of masonry buildings under horizontal loads. *Engineering Structures.* 2007;29(11):3134–3148.

5. Zucchini A., Lourenço P. B.. A micro-mechanical homogenisation model for masonry: Application to shear walls. *International Journal of Solids and Structures.* 2009;46(3-4):871–886.

6. Milani G.. Simple homogenization model for the non-linear analysis of in-plane loaded masonry walls. *Computers and Structures.* 2011;89(17-18):1586–1601.

7. Lotfi H. R., Shing P. B.. An appraisal of smeared crack models for masonry shear wall analysis. *Computers and Structures.* 1991;41(3):413–425.

8. Berto L., Saetta A., Scotta R., Vitaliani R.. An orthotropic damage model for masonry structures. *International Journal for Numerical Methods in Engineering.* 2002;55(2):127–157.

9. Pelà L., Cervera M., Roca P.. An orthotropic damage model for the analysis of masonry structures. *Construction and Building Materials.* 2013;41:957–967.

10. Psycharis I. N., Lemos J. V., Papastamatiou D. Y., Zambas C.. Numerical study of the seismic behaviour of a part of the Parthenon Pronaos. *Earthquake Engineering and Structural Dynamics.* 2003;32:2063–2084.

11. DeJong M. J., Dimitrakopoulos E. G.. Dynamically equivalent rocking structures. *Earthquake Engineering and Structural Dynamics.* 2014;43(10):1543-1563.

12. Bracchi S., Rota M., Penna A., Magenes G.. Consideration of modelling uncertainties in the seismic assessment of masonry buildings by equivalent-frame approach. *Bulletin of Earthquake Engineering.* 2015;13(11):3423–3448.

13. Rota M., Penna A., Magenes G.. A framework for the seismic assessment of existing masonry buildings accounting for different sources of uncertainty. *Earthquake Engineering and Structural Dynamics.* 2014;43(7):1045-1066.

14. Lagomarsino S., Penna A., Galasco A., Cattari S.. TREMURI program: An equivalent frame model for the nonlinear seismic analysis of masonry buildings. *Engineering Structures.* 2013;56:1787–1799.

15. Roca P., Molins C., Marí A. R.. Strength Capacity of Masonry Wall Structures by the Equivalent Frame Method. *Journal of Structural Engineering.* 2005;131(10):1601–1610.

16. Belmouden Y., Lestuzzi P.. An equivalent frame model for seismic analysis of masonry and reinforced concrete buildings. *Construction and Building Materials.* 2009;23(1):40–53.

17. Addessi D., Mastrandrea A., E. Sacco. An equilibrated macro-element for nonlinear analysis of masonry structures. *Engineering Structures.* 2014;70:82 - 93.

18. Parisi F., Augenti N.. Seismic capacity of irregular unreinforced masonry walls with openings. *Earthquake Engineering and Structural Dynamics.* 2013;42(1):101–121.

19. Quagliarini E., Maracchini G., Clementi F.. Uses and limits of the Equivalent Frame Model on existing unreinforced masonry buildings for assessing their seismic risk : A review. *Journal of Building Engineering.* 2017;10(March):166–182.

20. Mandirola M., Galasco A., Penna A., Magenes G.. Nonlinear macroelement modelling of experimental tests on masonry buildings with rigid diaphragms. Proceedings of the 16th International Brick and Block Masonry Conference; 2016; Padova.

21. Penna A., Senaldi I. E., Galasco A., Magenes G.. Numerical Simulation of Shaking Table Tests on Full-Scale Stone Masonry Buildings. *International Journal of Architectural Heritage.* 2016;10(2-3):146-163.

22. Cattari S., Chioccariello A., Degée H., Doneux C.. Seismic assessment of masonry buildings from shaking table tests and nonlinear dynamic simulations by the Proper Orthogonal Decomposition. 2nd European Conference on Earthquake Engineering and Seismology; 2014; Istanbul.

23. Kappos A. J., Penelis G. G., Drakopoulos C. G.. Evaluation of Simplified Models for Lateral Load Analysis of Unreinforced Masonry Buildings. *Journal of Structural Engineering.* 2002;128(7):890-897.

24. Siano R., Roca P., Camata G., et al. Numerical investigation of non-linear equivalent-frame models for regular masonry walls. *Engineering Structures.* 2018;173(July):512–529.

25. Penna A., Lagomarsino S., Galasco A.. A nonlinear macroelement model for the seismic analysis of masonry buildings. *Earthquake Engineering and Structural Dynamics.* 2014;43:159–179.

26. D'Ayala D. F., Paganoni S.. Assessment and analysis of damage in L'Aquila historic city centre after 6th April 2009. *Bulletin of Earthquake Engineering.* 2011;9(1):81–104.

27. Lagomarsino S.. Seismic assessment of rocking masonry structures. *Bulletin of Earthquake Engineering.* 2015;13:97–128.

28. DeJong M. J., Vibert C.. Seismic response of stone masonry spires: Computational and experimental modeling. *Engineering Structures.* 2012;40:566–574.

29. Malomo D., Pinho R., Penna A.. Using the Applied Element Method to simulate the dynamic response of full-scale URM houses tested to collapse or near-collapse conditions. 16th European Conference on Earthquake Engineering; 2018; Thessaloniki.

30. Tondelli M., Beyer K., DeJong M.. Influence of boundary conditions on the out-of-plane response of brick masonry walls in buildings with RC slabs. *Earthquake Engineering and Structural Dynamics.* 2016;45(8):1337–1356.

31. Caliò I., Marletta M., Pantò B.. A new discrete element model for the evaluation of the seismic behaviour of unreinforced masonry buildings. *Engineering Structures.* 2012;40:327–338.

32. Pantò B., Cannizzaro F., Caddemi S., Caliò I.. 3D macro-element modelling approach for seismic assessment of historical masonry churches. *Advances in Engineering Software.* 2016;97:40–59.

33. Raka E., Spacone E., Sepe V., Camata G.. Advanced frame element for the seismic analysis of masonry structures: model formulation and validation. *Earthquake Engineering and Structural Dynamics.* 2015;44:2489–2506.

34. Peruch M., Spacone E., Camata G.. Nonlinear analysis of masonry structures using fiber-section line elements. *Earthquake Engineering and Structural Dynamics.* 2019;48(12):1345-1364.

35. Peruch M., Spacone E., Shing P. B.. Cyclic Analyses of Reinforced Concrete Masonry Panels Using a Force-Based Frame Element. *Journal of Structural Engineering.* 2019;145(7):04019063.

36. McKenna F., Fenves G. L., Scott M. H., Jeremic B.. *Open System for Earthquake Engineering Simulation (OpenSees).* : Berkeley; 2000.

37. Magenes G., Calvi G. M.. In-plane seismic response of brick masonry walls. *Earthquake Engineering and Structural Dynamics.* 1997;26(11):1091–1112.

38. Turnšek V., Čačovič F.. Some experimental results on the strength of brick masonry walls. Proceedings of the 2nd International Brick Masonry Conference:149–156; 1971; Stoke-on-Trent, England.

39. Gambarotta L, Lagomarsino S. Damage models for the seismic response of brick masonry shear walls. Part I: the mortar joint model and its applications. *Earthquake Engineering and Structural Dynamics.* 1997;26:423–439.

40. Alfano G., Sacco E.. Combining interface damage and friction in a cohesive-zone model. *International Journal for Numerical Methods in Engineering.* 2006;68:542–582.

41. Vanin F., Zaganelli D., Penna A., Beyer K.. Estimates for the stiffness, strength and drift capacity tests reported in the literature. *Bulletin of Earthquake Engineering.* 2017;15(12):5435–5479.

42. Mann W., Muller H.. Failure of shear-stressed masonry. An enlarged theory, tests and application to shear walls. Proceedings British Ceramic Society Society; 1982.

43. Godio M., Vanin F., Zhang S., Beyer K.. Quasi-static shear-compression tests on stone masonry walls with plaster: influence of load history and axial load ratio (under review). *Engineering Structures.* 2019;:1–26.

44. Pfyl-Lang K., Braune F., Lestuzzi P.. *SIA D0237: Beurteilung von Mauerwerksgebäuden bezüglich Erdbeben.* : Zürich; 2011.

45. Petry S., Beyer K.. Influence of boundary conditions and size effect on the drift capacity of URM walls. *Engineering Structures.* 2014;65:76 - 88.

46. Wilding B. V., Beyer K.. Analytical and empirical models for predicting the drift capacity of modern unreinforced masonry walls. *Earthquake Engineering and Structural Dynamics.* 2018;47(10):2012–2031.

47. CEN . *Eurocode 8: Design of structures for earthquake resistance, Part 3: Assessmemt and retrofitting of buildings.* EN 1998-3: Brussels; 2005.

48. Giuffré A.. Seismic safety and strengthening of historical buildings and urban fabrics. 10th World Conference of Earthquake Engineering; 1994; Balkema, Rotterdam.

49. Doherty K., Griffith M. C., Lam N., Wilson J.. Displacement-based seismic analysis for out-of-plane bending of unreinforced masonry walls. *Earthquake Engineering and Structural Dynamics.* 2002;31:833–850.

50. Griffith M. C., Magenes G., Melis G., Picchi L.. Evaluation of out-of-plane stability of unreinforced masonry walls subjected to seismic excitation. *Journal of Earthquake Engineering.* 2003;7:141–169.

51. Godio M., Beyer K.. Tri-linear model for the out-of-plane seismic assessment of vertically-spanning unreinforced masonry walls. *submitted to ASCE Structural Engineering Journal.* 2017;.

52. Derakhshan H., Griffith M. C., Ingham J. M.. Out-of-Plane Behavior of One-Way Spanning Unreinforced Masonry Walls. *Journal of Engineering Mechanics.* 2013;139(4):409–417.

53. Housner G. W.. The behavior of inverted pendulum structures during earthquakes. *Bullettin of the Seismological Society of America.* 1963;53(2):403–417.

54. Makris N., Konstantinidis D.. The rocking spectrum and the limitations of practical design methodologies. *Earthquake Engineering and Structural Dynamics.* 2003;32(2):265–289.

55. Vassiliou M. F., Mackie K. R., Stojadinović B.. A finite element model for seismic response analysis of deformable rocking frames. *Earthquake Engineering and Structural Dynamics.* 2017;46(3):447–466.

56. Vassiliou M. F., Mackie K. R., Stojadinović B.. Dynamic response analysis of solitary flexible rocking bodies: modeling and behavior under pulse-like ground excitation. *Earthquake Engineering and Structural Dynamics.* 2014;43(10):1463–1481.

57. Petrini L., Maggi C., Priestley M. J. N., Calvi G. M.. Experimental verification of viscous damping modeling for inelastic time history analyses. *Journal of Earthquake Engineering.* 2008;12:S1:125–145.

58. Hall J. F.. Problems encountered from the use (or misuse) of Rayleigh damping. *Earthquake Engineering and Structural Dynamics.* 2006;35:525–545.

59. Peña F., Lourenço P. B.. Modeling the dynamic behaviour of masonry walls as rigid blocks. *Computational Mechanics.* 2006;(June):5–8.

60. Sorrentino L., AlShawa O., Decanini L. D.. The relevance of energy damping in unreinforced masonry rocking mechanisms. Experimental and analytic investigations. *Bulletin of Earthquake Engineering.* 2011;9:1617–1642.

61. Degli Abbati S., Lagomarsino S.. Out-of-plane static and dynamic response of masonry panels. *Engineering Structures.* 2017;150:803–820.

62. ElGawady M. A., Ma Q., Butterworth J. W., Ingham J.. Effects of interface material on the performance of free rocking blocks. *Earthquake Engineering and Structural Dynamics.* 2011;:375–392.

63. Degli Abbati S., Rossi M., Lagomarsino S.. Out-of-plane experimental tests on masonry panels. 2nd European Conference on Earthquake Engineering and Seismology; 2014; Instanbul.

How to cite this article: Vanin F., Penna A., Beyer K. (2019), A three-dimensional macroelement for modelling of the in-plane and out-of-plane response of masonry walls, *submitted to Earthquake Engineering & Structural Dynamics, HHH.*